Acta Pharmaceutica Sinica B 2021;11(4):1069−1082

Chinese Pharmaceutical Association
Institute of Materia Medica, Chinese Academy of Medical Sciences

Acta Pharmaceutica Sinica B

www.elsevier.com/locate/apsb
www.sciencedirect.com

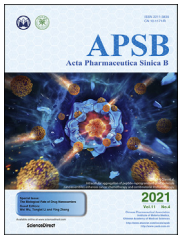

SHORT COMMUNICATION

Intracellular aggregation of peptide-reprogrammed small molecule nanoassemblies enhances cancer chemotherapy and combinatorial immunotherapy

Jinrong Peng, Yao Xiao, Qian Yang, Qingya Liu, Yu Chen, Kun Shi, Ying Hao, Ruxia Han, Zhiyong Qian*

State Key Laboratory of Biotherapy and Cancer Center, West China Hospital, Sichuan University, And Collaborative Innovation Center of Biotherapy, Chengdu 610065, China

Received 5 March 2020; received in revised form 15 April 2020; accepted 5 June 2020

KEYWORDS

Nanoassembly;
Glutathione response;
Intracellular aggregation;
Chemotherapy;
Combinational immunotherapy

Abstract The intracellular retention of nanotherapeutics is essential for their therapeutic activity. The immobilization of nanotherapeutics inside target cell types can regulate various cell behaviors. However, strategies for the intracellular immobilization of nanoparticles are limited. Herein, a cisplatin prodrug was synthesized and utilized as a glutathione (GSH)-activated linker to induce aggregation of the cisplatin prodrug/IR820/docetaxel nanoassembly. The nanoassembly has been reprogrammed with peptide-containing moieties for tumor-targeting and PD-1/PD-L1 blockade. The aggregation of the nanoassemblies is dependent on GSH concentration. Evaluations *in vitro* and *in vivo* revealed that GSH-induced intracellular aggregation of the nanoassemblies enhances therapeutic activity in primary tumors by enhancing the accumulation and prolonging the retention of the chemotherapeutics in the tumor site and inducing reactive oxygen species (ROS) generation and immunogenic cell death. Moreover, the nanoassemblies reinvigorate the immunocytes, especially the systemic immunocytes, and thereby alleviate pulmonary metastasis, even though the population of immunocytes in the primary tumor site is suppressed due to the enhanced accumulation of chemotherapeutics. This strategy provides a promising option for the intracellular immobilization of nanoparticles *in vitro* and *in vivo*.

*Corresponding author.
E-mail addresses: anderson-qian@163.com, zhiyongqian@scu.edu.cn (Zhiyong Qian).

Peer review under responsibility of Chinese Pharmaceutical Association and Institute of Materia Medica, Chinese Academy of Medical Sciences.

https://doi.org/10.1016/j.apsb.2020.06.013

2211-3835 © 2021 Chinese Pharmaceutical Association and Institute of Materia Medica, Chinese Academy of Medical Sciences. Production and hosting by Elsevier B.V. This is an open access article under the CC BY-NC-ND license (http://creativecommons.org/licenses/by-nc-nd/4.0/).

© 2021 Chinese Pharmaceutical Association and Institute of Materia Medica, Chinese Academy of Medical Sciences. Production and hosting by Elsevier B.V. This is an open access article under the CC BY-NC-ND license (http://creativecommons.org/licenses/by-nc-nd/4.0/).

1. Introduction

Beyond the enhanced permeability and retention (EPR) effect, further enhancement of nanoparticle retention inside tumors or tumor cells has a critical role in the therapeutic outcome of nanomedicine and in cellular behaviors[1,2]. Shape- or size-transformable or responsive nanoparticles have been developed to enhance the intratumoral penetration of cargos, and the delivery efficacy has also been improved[3−6]. Unfortunately, the use of nanomedicines is still limited by their modest therapeutic activity and the difficulty in prolonging their intratumoral persistence due to the enhanced interstitial pressure inherent in solid tumors and the limited accumulation inside tumor cells, as well as to the gradual dissociation of the cargo carriers, which may further result in drug resistance[7−10]. Prolonging the lifetime of nanoparticles (nanomedicines) and immobilizing them inside the targeted cell type—*e.g.*, cancer cells, macrophages, or erythrocytes—have emerged as potential strategies to enhance their therapeutic use in cancer, especially in chemotherapy (to directly prolong the exposure time of cancer cells to chemotherapeutics) or immunotherapy (to potentially regulate cell behaviors), which are as important as strategies to enhance the accumulation of nanoparticles in tumor sites[11−14]. More importantly, the intracellular aggregation of nanoparticles can regulate cell behaviors, for example, overcoming drug resistance[15].

Consequently, several strategies and nanosystems have been developed. Responsive peptides are potential choices. Their residues can be induced to assemble into nanofibers or accumulate in specific cellular sites, *e.g.*, the cell membrane[16−18]. In addition, when activated by specific enzymes or extracellular stimuli, the residues can cross-link with each other and enhance the retention of the residues inside the tumor[19−21]. In addition to these strategies, inducing intracellular nanoparticles to undergo flocculation may be an alternative. Flocculation is a normal phenomenon in particle-based dispersion and sometimes occurs in unstable nanoparticle systems as a result of failed nanoparticle construction due to immature techniques. Flocculation results in aggregation and favors the immobilization of nanoparticles *in vivo*. Numerous factors, including materials, construction techniques, and the surrounding microenvironment, affect this aggregation process. Among these factors, alterations in the medium environment exhibit great potential for inducing controllable aggregation because the unique and ubiquitous characteristics of the tumor microenvironment—*e.g.*, the influences of acidic, hypoxic and high redox potential environments—are well known and studied[22]. In contrast to acidity, the high levels of glutathione (GSH) produced intracellularly to maintain a high redox environment may provide a suitable switch, controller or stimulus to achieve intracellular aggregation of nanoparticles due to the sharp gradient of GSH from the intercellular environment to the cytoplasm in tumor tissue[23,24]. For this strategy, a GSH-responsive molecule or system to induce aggregation inside tumor cells is required. In addition, the molecule or system must be able not only to react with GSH but also to subsequently induce aggregation.

Numerous prodrugs have been developed[25], among which cisplatin prodrugs are promising candidates[26]. After modification, *e.g.*, by hexanoic acid, the obtained cisplatin prodrug (IV) can react with GSH to generate hydroxylated cisplatin (IV) or cisplatin (II); subsequently, the released hydroxylated cisplatin can still react with mercapto groups[27−29]. This ability enables the molecular mechanism of GSH-triggered intracellular aggregation. More importantly, the reaction rate between GSH and cisplatin prodrugs can be altered by modification. The electron-withdrawing potential steers the reaction. However, most cisplatin prodrugs are hydrophobic, limiting their bioavailability and lowering their accumulation in tumor sites.

In our previous study, we developed a nanoassembly system fully formed by small molecules. This nanoassembly system can be reprogrammed by functional peptides and can achieve enhanced tumor-targeting and chemo-photothermal-immunotherapeutic effects[30]. Among the small molecules forming the nanoassembly, *N*,*N*′-bis(acryloyl)cystamine (BISS) is a critical component for the reconstruction of nanoassembly by peptides. Moreover, the chemical structure of BISS contains a −S−S− bond, which can be broken by GSH to generate free mercapto groups. Therefore, this nanoassembly system provides an inherent GSH-responsive group to achieve aggregation by reacting with released hydroxylated cisplatin. The reaction between intracellular reductants and platinum-based chemotherapeutics is the main reason that the therapeutics fail *in vivo* validation. Exploiting this feature and codelivering other therapeutics may offer a suitable strategy to achieve the prolonged retention of nanomedicines and cell behavioral alterations *via* GSH-triggered aggregation, thus enhancing chemotherapy and combinatorial immunotherapy.

Therefore, in this study, we first synthesized cisplatin prodrugs by modifying them with two kinds of molecules with different electron-withdrawing potentials. Then, we coassembled them with other components, including BISS and docetaxel (DTX), to form a nanoassembly, which was finally reprogrammed with a multifunctional peptide. The potential of this nanoassembly in GSH-induced aggregation and enhanced chemotherapy and consequently in combinational immunotherapy have also been evaluated in detail (Scheme 1).

2. Methods and experimental

2.1. Materials

2.1.1. Chemical reagents

Hydrogen peroxide, ethanol, and GSH, etc. were purchased from Aladdin, Shanghai, China. Hexanoic anhydride, heptafluorobutyric anhydride, R820 dye, acetonitrile, *N*,*N*′-bis(acryloyl)cystamine

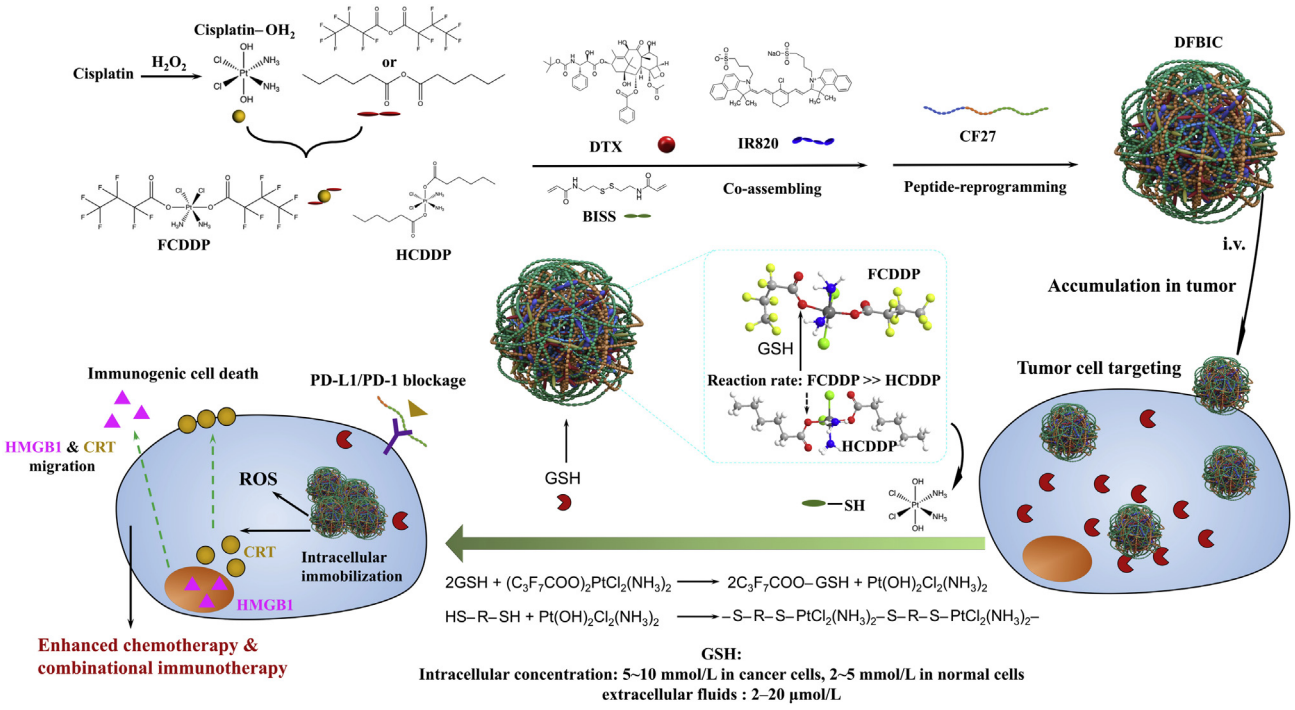

Scheme 1 Small molecules nanoassemblies-induced aggregation achieves intracellular immobilization of drug-loaded nanoassemblies. In cancer cells, the immobilization of nanoassemblies prolongs the localization of therapeutics inside tumor cells and changes the cell behaviors, *e.g.*, turning the cell apoptosis to immunogenic cell death, thus realizing enhanced immunotherapy, which favors the enhancement of combinational therapy.

(BISS), DAPI, coumarin-6, and rhodamine, etc. were all purchased from Sigma–Aldrich, Merck, Darmstadt, USA. Cisplatin, docetaxel, and resiquimod (R848), etc. were purchased from MedChemExpress (MCE), New Jersey, USA. CF27 peptide was customized from ChinaPeptides Co., Ltd., Shanghai, China. Antibodies and recombined proteins: αCD3 (CD3-FITC monoclonal antibody, catalog: 11-0032-80), αCD4 (CD4-APC monoclonal antibody, catalog: 17-0041-82), αCD8 (CD8a-PE-cyanine 7 monoclonal antibody, catalog: 25-0081-82), (eBioscience, Invitrogen, Thermo Fisher Scientific, Massachusetts, USA); αCD68 (CD68 monoclonal antibody (FA-11), Alexa Fluor 488, catalog: ab201844), αiNOS (iNOS monoclonal antibody (EPR16635), Alexa Fluor 647, catalog: ab209027), αCD206 (mannose receptor monoclonal antibody (EPR6828(B), Alexa Fluor 647, catalog: ab195192), (Abcam, Cambridge, England); αCRT (calreticulin, Calreticulin (D3E6) XP Rabbit mAb, catalog: 12238T, Cell Signaling Technology, Danvers, USA); αHMGB1 (high mobility group protein 1) (human/mouse HMGB1/HMG-1 antibody, catalog: MAB16902-SP; NorthernLightTM 557-conjugated anti-mouse IgG secondary antibody, catalog: NL007, R&D System, Minnesota, USA); αIFN-γ and αPD-L1 for IHC were provided by Servicebio (Wuhan Goodbio Technology CO., Ltd., Wuhan, China); Treg Flow Kit (True-Nuclear one step staining mouse Treg Flow kit (FOXP3 Alexa FluorR 488/CD25 PE/CD4 PerCP), Biolegend, San Diego, USA); CBA kit (mouse inflammation kit (content: IL-6, IL-10, MCP1, IFN-γ, TNF-α and IL-12p70, BD Biosciences, catalog: 552364, San Jose, USA); recombined IL-4, recombined IFN-γ, LPS, etc. were purchased from Biolegend (San Diego, USA).

2.1.2. *Cell lines*

4T1, 4T1-Luciferase, MDA-MB-231, HCT8 (PTX resistance), RAW 264.7, were purchased from cell bank of CAS (Shanghai, China), which were all originated from American Type Culture Collection (ATCC, Rockville, MD, USA).

2.1.3. *Animals*

BALB/c mice (HFK Bioscience Co., Ltd., Beijing, China). Kept under specific-pathogen-free condition with free access to standard food and water. All animal procedures were performed following the protocols approved by the Institutional Animal Care and Treatment Committee of Sichuan University (Chengdu, China).

2.2. *Synthesis of cisplatin prodrugs*

Before the synthesis of $Pt(NH_3)_2Cl_2(O_2CCH_2CH_2CH_2CH_2CH_3)_2$ or $Pt(NH_3)_2Cl_2(O_2CCF_2CF_2CF_3)_2$, *cis*,*trans*,*cis*-$[PtCl_2(OH)_2(NH_3)_2]$ was first synthesized based on that previous described[31]. After recrystallized and washed and dried, a solution of *cis*,*trans*,*cis*-$[PtCl_2(OH)_2(NH_3)_2]$ in DMSO was prepared, and then mixed with hexanoic anhydride or heptafluorobutyric anhydride and the mixture was kept stirring for 48 h before the addition of pre-colded water to obtain precipitate. And the precipitate was purified by washing with acetonitrile and diethyl ether and dried in vacuum. The obtained $Pt(NH_3)_2Cl_2(O_2CCH_2CH_2CH_2CH_2CH_3)_2$ (HCDDP) or $Pt(NH_3)_2Cl_2(O_2CCF_2CF_2CF_3)_2$ (FCDDP) was stored in dark for further applications.

2.3. *Preparation of peptide-modified small molecules nanoassemblies*

The peptide modified small molecules nanoassemblies were prepared based on our previous study with some modification. Briefly, to a certain volume of aqueous solution of IR820 (1 mg/mL) under

stirring, a solution of DTX/FCDDP/BISS or DTX/HCDDP/BISS or DTX/BISS or FCDDP/BISS or HCDDP/BISS in DMSO was added. Several minutes later, a volume of aqueous solution of peptide-CF27 was added dropwise. The mixture solution was kept stirring for 1 h. Then the mixture was transferred to dialysis bag (molecular cutoff: 1000 Da) and dialyzed against to water (18.5 MΩ) for 24 h (the water was changed every 3−4 h). The obtained nanoassemblies were characterized by UV−Visible spectrometer, DLS, nanoparticle tracking system, and TEM, etc.

2.4. Characterization of prodrugs and nanoassemblies

2.4.1. Chemical structure

The synthesized FCDDP and HCDDP were characterized by ^{1}H NMR, ^{13}C NMR, and ^{19}F NMR (Bruker AV II-600 MHz, German). All the samples were dissolved in DMSO-d_6.

2.4.2. Binding energy

The binding energy of the obtained FCDDP and HCDDP were characterized by X-ray photoelectron spectroscopy (XPS, AXIS Ultra DLD, Kratos, UK).

2.4.3. Particle morphology

The morphological investigation of the obtained nanoassemblies were observed by Transmission Electron Microscope (TEM). Before TEM observation, each sample was dropped on a grid with carbon film and dried in room temperature.

2.4.4. Surface morphology

The surface morphology and element distribution of the nanoassemblies were conducted by scanning electron microscope (SEM). The nanoassemblies were lyophilized before SEM observation without novel metal spraying.

The sample preparation for TEM and SEM observation followed the procedure of the previous studies[30].

2.4.5. Size distribution and zeta potential

The real-time hydrodynamic dimeters and the anti-diluted performance of the nanoassemblies were measured by real-time nanoparticle tracking system (Zeta View, NTA, Particle Metrix, Germany). And the zeta potential was detected by dynamic laser scattering (DLS, Zetasizer nano ZS, Malvern, UK).

2.4.6. Optical properties

The optical properties including light absorption and fluorescent potential were measured by UV-visible spectrometer (UV−Vis spectrophotometer, UV-2600, SHIMADZU, Japan) and fluorescent spectrometer (Spectro Fluorophotometer, RF-6000, SHIMADZU, Japan), respectively.

2.5. GSH-induced aggregation of nanoassemblies

2.5.1. Effect of GSH concentration onto the aggregation formation

The obtained nanoassemblies were added into the mediums with the final concentration of GSH at 10, 5, 2.5, 1 and 0 mmol/L. The concentration nanoassemblies (DTX) were settled at 100 ug/mL. The samples were shacked at the rate of 45 rpm at 25 °C. At predetermined time-point, stopped shaking and maintained for 3 h to fully precipitate and took the photos.

2.5.2. Effect of nanoassembly concentration onto the aggregation formation

Similar procedure was conducted, settled the final GSH concentration at 10 mmol/L, and the nanoassemblies concentration (DTX) varied from 50 to 25, 12.5, 6.25, 3.12, 1.56 and 0 μg/mL.

2.6. Aggregation of nanoassemblies in vitro

Fluorescent imaging of the cancer cells was utilized to evaluate the aggregation of nanoassemblies *in vitro*. Coumarin 6 (C6) and camptothecin (CPT) were used as the fluorescent dye for the substitutes of the drugs. A small amount of C6 and CPT were co-loaded into the nanoassemblies. The cancer cells (4T1 cancer cells) were incubated with dyes-loaded nanoassemblies. And 8 h later, the cancer cells were washed by PBS and fixed with paraformaldehyde and further stained with DAPI. The fluorescent images were obtained from confocal fluorescence microscopy (Zeiss 880+ Airyscan, Carl Zeiss, Jena, German). And the fluorescent intensity of the taken images were analyzed by Image J software.

2.7. Cytotoxicity of nanoassemblies

Several cancer cell lines were used to evaluate the cytotoxicity of obtained nanoassemblies, which including triple negative breast cancer cell lines−4T1 breast cancer cell (4T1 and 4T1-Luciferase) and MDA-MB-231 cancer cell and HCT8 (PTX resistance). The cell culturing procedure and cell survival measurement were performed as our previous report. The samples for assessment include DBIC, DFBIC, DFBI, DHBIC, HBIC, DFHBIC, free DTX, and free cisplatin, etc. MTT assays were conducted to evaluate the mean cell survival.

Beyond the cytotoxicity, we further evaluated the effect of nanoassemblies onto the apoptosis behavior of the cancer cells, especially to the induction of immunogenic cell death. After being co-cultured with nanoassemblies, the cancer cells were washed by PBS and fixed with paraformaldehyde, then stained with αCRT and αHMGB1. The fluorescent images of the cancer cells were captured by confocal fluorescence microscopy and analyzed by Image J software. The localization of the fluorescence dye anchored to the antibodies can be used as the indirectly indicator of the migration of CRT and HMGB1.

2.8. Tumor-targeting in vivo and aggregation of nanoassemblies in vivo

In order to evaluate the tumor targeting of nanoassemblies, 4T1 breast cancer model was established on BALB/c mice. In brief, 1×10^6 4T1 breast cancer cells were subcutaneously injected to the right flank of the mice. While the tumor volume reached to $\sim$100 mm^3 (6 mm × 6 mm), the mice were divided into several groups and treated with free IR820, DBIC, DFBIC, DFBI, etc. IR820 was used as the fluorescent dye. The IR820 itself can be served as the NIR fluorescent dye. And the 4T1-Lu cell line was used for bioluminescence imaging to evaluate the tumor growth *in vivo*. And the fluorescent dye distribution was measured by living fluorescent imaging systems (IVIS, PerkinElmer, USA, excitation = 740 nm, emission = 790 nm long pass). At a predetermined time-point, the mice were anesthetized to death, and the major organs and tumor tissues were eviscerated for *ex vivo* fluorescent imaging.

Moreover, in another parallel assay, after the mice were treated with nanoassemblies co-loaded with fluorescent dye-C6 and rhodamine, at settled time-points, the tumor tissues were eviscerated after the mice were anesthetized to death, and then frozenly sliced up and stained with DAPI. The frozen slices were used to evaluate the *in vivo* formation of aggregation by fluorescent imaging.

2.9. Anti-cancer performance of nanoassemblies in vivo

Two assays were conducted to evaluate the anti-cancer performance of nanoassemblies *in vivo*. The difference of these two assays was the tumor volumes while the treatment initiated: one is ~100 mm^3 (6 mm × 6 mm) and the other is ~250 mm^3 (8 mm × 8 mm). In brief, 1×10^6 of 4T1 breast cancer cells were subcutaneously injected into the right flank of the mice, while the average tumor volume reached to ~100 mm^3, the mice were divided into several groups and treated with saline, free DTX/cisplatin, DFBI, DBIC, DFBIC, DFBIC+Laser and FBIC, respectively (6 mice per group). The tumor volume and body weight of the mice were measured and recorded twice a week. At predetermined time-points and at day 22 after the first treatment was administrated, the mice were anesthetized to death and the tumor tissues were eviscerated for photographing and pathological analysis after being stained with specific antibodies, respectively.

In other assays, while the dimension of tumors grown to 8 mm × 8 mm, the mice were divided into four groups and treated with saline, DFBI, DBIC, and DFBIC, respectively. The purpose of this assay was to evaluate the effect of nanoassemblies onto the alleviation of pulmonary metastasis. The tumor volume and body weight were measured and recorded every twice a week. At predetermined time-points and at Day 22, after the mice were anesthetized to death, the lung tissues and tumors were eviscerated and the metastasis and metastatic nodes on the lung tissues were calculated and recorded, respectively. Then all the tissues were fixed by paraformaldehyde for pathological analysis, especially for the identification of pulmonary metastasis.

2.10. Mechanism studying of enhanced immunotherapy and pathological analysis

We further evaluated the effect of nanoassemblies-mediated treatment onto the stimulation of immune response inside tumor. The tumor tissues were stained by a series of antibodies to semiquantitatively identify several immune related biomarkers, which including PD-L1, CD3, CD4, CD8, IFN-γ and CD68. In flow cytometry assay, the fresh eviscerated tumor tissues were treated according to previous report[30]. And the obtained cell suspension was stained with αCD3-FITC (Invitrogen, catalog: 11-0032-80, clone: 17A2), αCD8α-PE-cyanine (Invitrogen, catalog: 25-0081-82, clone: 53−6.7), αCD4-APC (Invitrogen, catalog: 17-0041-82, clone: GK1.5) antibodies according to the manufacture's protocols, and the proportion of the T cells were measured by flow cytometry. In the immunofluorescent staining assays, the tumor slices were stained with DAPI and αCD8/αIFN-γ or DAPI and αCD68. The variation of PD-L1 expression was detected by immunohistochemical staining. And the apoptosis of the cancer cells was evaluated by TUNEL assays. Furthermore, the pulmonary metastasis and pathological changes of the major organs were investigated by H&E staining of the tissues.

2.11. Statistical analysis

Statistical analysis was performed using SPSS 15.0 software (IBM Corporation, Armonk, NY, USA). The results were indicated as mean ± SD. Analysis of variance was employed for multiple group comparisons, and results of $P < 0.05$ were considered statistically significant.

3. Results and discussion

3.1. Preparation and characterization of nanoassemblies

Before the construction of the peptide-reprogrammed small-molecule nanoassembly, we prepared two kinds of cisplatin prodrugs, fluorinated cisplatin (FCDDP) and alkylated cisplatin (HCDDP), which were obtained after the reaction of CDDP with heptafluorobutyric anhydride and hexanoic anhydride, respectively. By ^{1}H NMR and ^{19}F NMR plus XPS, we confirmed the successful synthesis of these prodrugs (Supporting Information Fig. S1). Then, the peptide-reprogrammed small-molecule nanoassembly was prepared according to the procedure used in our previous study[26] with minor modifications (Supporting Information Fig. S2). Without the introduction of the peptide, small molecules, including DTX, FCDDP or HCDDP, IR820, and BISS, self-assembled into nanoparticles ~30 nm in diameter (named DFBI or DHBI as appropriate, Fig. 1A1). The driving force for the formation of the nanoassembly is hydrophobic−hydrophobic assembly. IR820 contains a hydrophilic sulfonic acid group and hydrophobic backbone. It serves as an amphiphilic molecule to induce the assembly of hydrophobic cisplatin prodrugs and hydrophobic chemotherapeutics. The underlying mechanism has been illustrated in our previous study[30]. With the involvement of the peptide, named CF27, in the preparation process, the nanoparticles were transformed to a core−shell nanoassembly (named DFBIC) with a uniform distribution and a diameter of ~20 nm (Fig. 1A2). We further dispersed the nanoassembly into serum buffer (10% fetal bovine serum). The results indicated that the nanoassembly maintained its hydrodynamic diameter [detected by DLS, 35 ± 5.8 nm (0 h) to 38 ± 6.2 nm in number%] for 24 h and increased to 43 ± 4.9 nm 48 h later, indicating that the nanoassembly is relatively stable in serum buffer (Supporting Information Fig. S3). In addition, no obvious therapeutic component aggregation was observed by SEM-EDS mapping (Supporting Information Fig. S4). The morphological differences provided nanoassemblies with distinguishable antidilution performance.

We further tested the critical micellar concentration/critical aggregation concentration (CMC/CAC) of the drug-loaded nanoassembly by a digital conductivity meter combined with a fluorescence spectrophotometer. The results revealed that the CMC/CAC of the nanoassembly was 5.2×10^{-5} mol/L IR820 (44.2 μg/mL, IR820:DTX was 6:5, Supporting Information Fig. S5). The concentration of the prepared nanoassembly was 0.6 mg/mL (IR820). When DFBI nanoparticles were diluted 1000-fold, almost no particles could be found by the nanoparticle tracking system; in contrast, even after 4000-fold dilution, DFBIC nanoassemblies could be detected easily and retained a narrow hydrodynamic diameter distribution (Fig. 1B and Supporting Information Fig. S6). This further supports the antidilution potential of the DFBIC nanoassembly. The zeta potentials of the nanoassemblies (DFBI or DFBIC) were similar to that of free IR820 in aqueous solution, ranging from

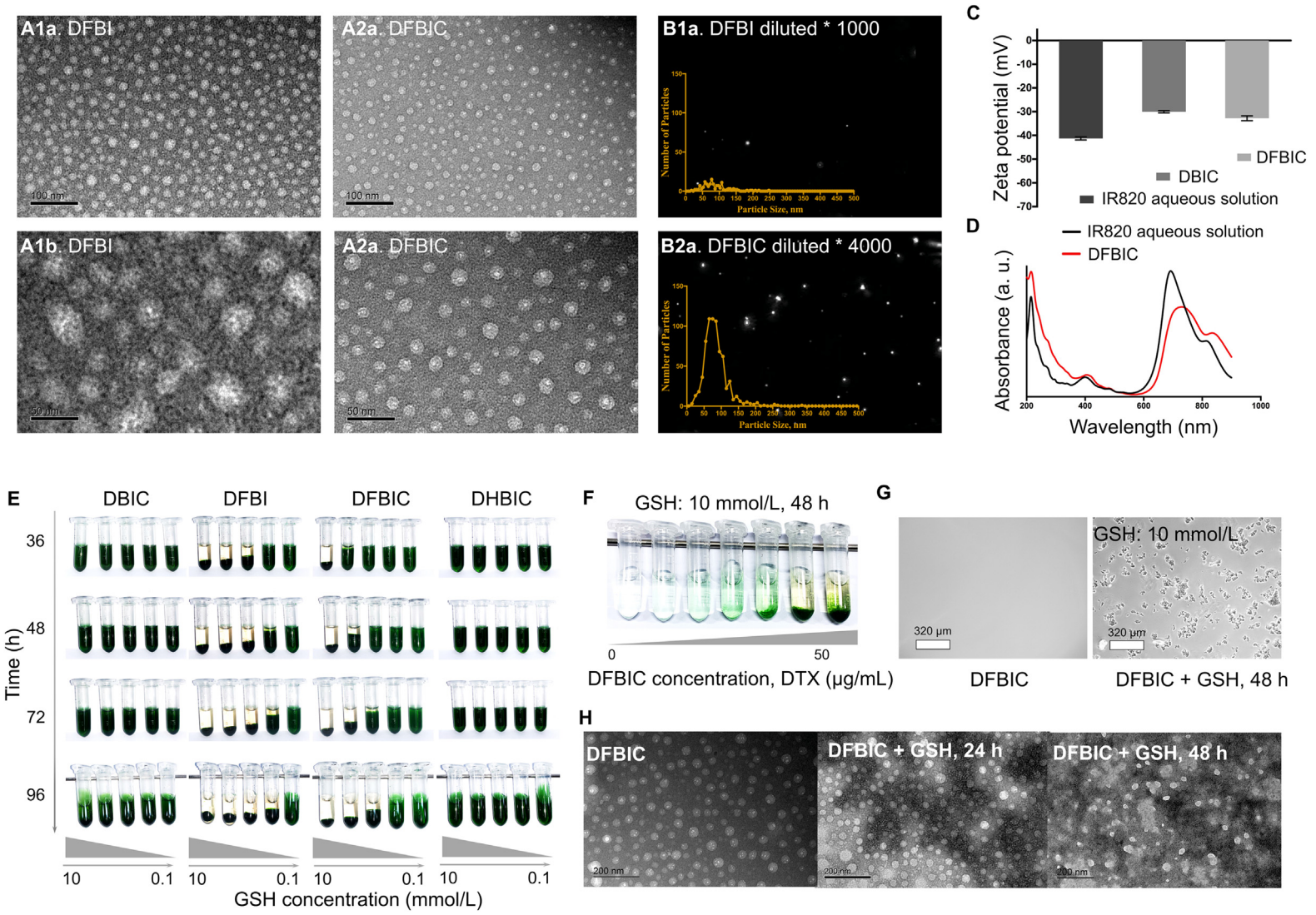

Figure 1 (A)−(D) Characterization of nanoassemblies. (A) TEM images of DFBI and DFBIC. (B) Nanoparticle size distributions of DFBI and DFBIC measured by nanoparticle tracking system ($n = 3$). (C) Zeta potentials of nanoassemblies detected by DLS ($n = 3$). (D) UV−Visible spectra of nanoassemblies. (E−H) GSH-induced aggregation of nanoassemblies. (E) Effect of GSH concentration onto the aggregation of nanoassemblies, which including DBIC, DFBI, DFBIC, and DHBIC. (F) Effect of nanoassemblies concentration onto the aggregation of nanoassemblies. (G) Microscopy observation of the aggregation of nanoassemblies. (H) TEM images captured to evaluate the morphological changes of the nanoassemblies with the presence of GSH.

−40 to −30 mV (Fig. 1C). The negative charge on the surface favors prolongation of the circulating time of the nanoassembly *in vivo*[32−34]. After the formation of the nanoassembly, the absorption of IR820 in the near infrared (NIR) region was redshifted, which also indicated the assembly of the small molecules[35]. In addition, the absorption of the drugs (in the wavelength range of 200−400 nm) further enhanced the absorption of the system in the UV−Visible spectra, further demonstrating the incorporation of the small-molecule drugs into the nanoassembly (Fig. 1D).

3.2. *GSH-induced aggregation of nanoassemblies*

Then, nanoassemblies were prepared with different components, including DBIC (without the cisplatin prodrug), DFBI (with FCDDP), DFBIC (with FCDDP), and DHBIC (with HCDDP), to evaluate the potential of the small-molecule nanoassemblies in inducing GSH-triggered aggregation. The obtained nanoassemblies were dispersed in media containing different concentrations of GSH. No aggregation was detected in the DBIC or DHBIC dispersions with GSH concentrations ranging from 0 to 10 mmol/L. In contrast, obvious aggregation was observed in the DFBI and DFBIC dispersions. This pattern indicates that the involvement of cisplatin prodrugs, especially FCDDP, is critical to aggregation. As the concentration of GSH increased, aggregation occurred more obviously and quickly, especially when the GSH concentration was higher than 5 mmol/L in the DFBIC dispersion (for DFBI, the threshold GSH concentration was lower than 2.5 mmol/L, Fig. 1E). This finding indicates that the aggregation rate of the nanoassembly can be controlled by the GSH concentration. In addition, the concentration of the nanoassembly influenced the aggregation process. When the concentration of DTX in the DFBIC aqueous dispersion was decreased from 50 to ∼6 μg/mL, obvious aggregation was observed after 48 h of incubation in the presence of 10 mmol/L GSH (Fig. 1F). When the DFBIC concentration was further decreased to ∼3 μg/mL (DTX concentration), aggregation was still observed by microscopy (Fig. 1G). In addition, the nanoassemblies prepared without the addition of BISS (DFIC) did not induce aggregation in the presence of various GSH concentrations (Supporting Information Fig. S7). This result demonstrates that aggregation of the nanoassembly occurs even when the concentration of the nanoassembly is relatively low (several μg/mL), and FCDDP and BISS are the necessary components for aggregation. The main driving force for the aggregation is the GSH concentration. Pt−S interaction induced crosslinking of the nanoassemblies. After the interaction between the cisplatin prodrug and GSH, the −SH reactive Pt-based molecule is released, and the BISS contained in the nanoassembly also generates free −SH, thus inducing the formation of Pt−S crosslinking and consequent aggregation. We further evaluated the morphological change during the aggregation process. When the nanoassemblies were placed in medium containing GSH, the core−shell morphology [white−gray in the transmission electron microscopy (TEM) image] was disrupted, and some crystal structures (dark-black in the TEM image) were found around the nanoassemblies 24 h later (Supporting Information Fig. S8). As the incubation time was extended, links (dark black−gray) were formed among the nanoparticles (white in the TEM image, Fig. 1H). From previous reports, we conclude that GSH can react with the ester bond formed in the cisplatin prodrugs. In addition, by calculating the charge distribution across the prodrug molecules, we found that the charge on the carbon atom of the C═O bond in FCDDP is more positive than that in HCDDP (Supporting Information Fig. S9). Thus, GSH is more likely to react with FCDDP than with HCDDP, which may be the main reason that the cytotoxicity of FCDDP was lower than that of HCDDP in the subsequent MTT assays. After the reaction between GSH and FCDDP, hydroxylated cisplatin was released, as confirmed by drug release assays (Supporting Information Fig. S10). Additionally, the S−S bond introduced from BISS was broken by GSH, further providing a sufficient amount of free mercapto groups. The mercapto groups have a high reaction affinity for hydroxylated cisplatin to form −S−Pt− bonds, which is not only the main cause of the attenuated cytotoxicity of Pt-based therapeutics[29] but also the reason for the aggregation of nanoassemblies. The breakage of the S−S bond is also the main reason for the further release of cisplatin into the medium. In addition, the FCDDP was released rapidly from the nanoassemblies constructed without the introduction of BISS (DFIC group) in the buffer in the absence of GSH (Fig. S10). Without the introduction of BISS, no reaction could take place between the peptide and the nanoassemblies to form peptide-reprogrammed nanoassemblies, which makes DFIC only a mixture of DFI and the peptide, an unstable nanoassembly structure. This indicates the important role of BISS in the construction of nanoassemblies.

From the 2D fluorescent spectra of the nanoassemblies with GSH, we also found disruption of the nanoassemblies. The fluorescent spectrum of DFBIC with GSH became similar to that of free IR820, demonstrating the dissociation of the nanoassemblies and the release of IR820 (Supporting Information Fig. S11). Furthermore, IR820 is an efficient photosensitizer for photothermal therapy. The aggregation may also change the photothermal conversion of the nanoassemblies. After aggregation, under irradiation with an 808 nm laser, the temperature of the aggregated nanoassemblies increased to 52 °C in 1 min, while the nanoassembly dispersion was 33 °C (Supporting Information Fig. S12). This demonstrates that the NIR dyes were also concentrated after aggregation, which resulted in enhanced topical photothermal conversion. It also provides a strategy for enhanced photothermal therapy.

3.3. *Intracellular aggregation of nanoassemblies in vitro and in vivo*

3.3.1. *Intracellular aggregation in vitro*

Furthermore, we evaluated intracellular aggregation of the small-molecule nanoassemblies *in vitro* and *in vivo*. 4T1 breast cancer cells were selected, and two fluorescent dyes, camptothecin (CPT) and coumarin 6 (C6), were introduced. After incubation with the nanoassembly for 8 h, aggregation [visualized with bright fluorescence of both CPT and C6; and the blue fluorescence in the nucleus was the DAPI dye, and no CPT was detected in the nucleus, as confirmed after further evaluation (Supporting Information Fig. S13)] was observed in cancer cells treated with DFBIC but not in those treated with DBIC (Fig. 2A). Unsurprisingly, aggregation occurred much faster in these cellular assays than in the biochemical assays, indicating that aggregation can be triggered not only by GSH but also by intracellular substances and that the high redox environment inside tumor cells may have a critical impact on aggregation. Then, we investigated the effect of

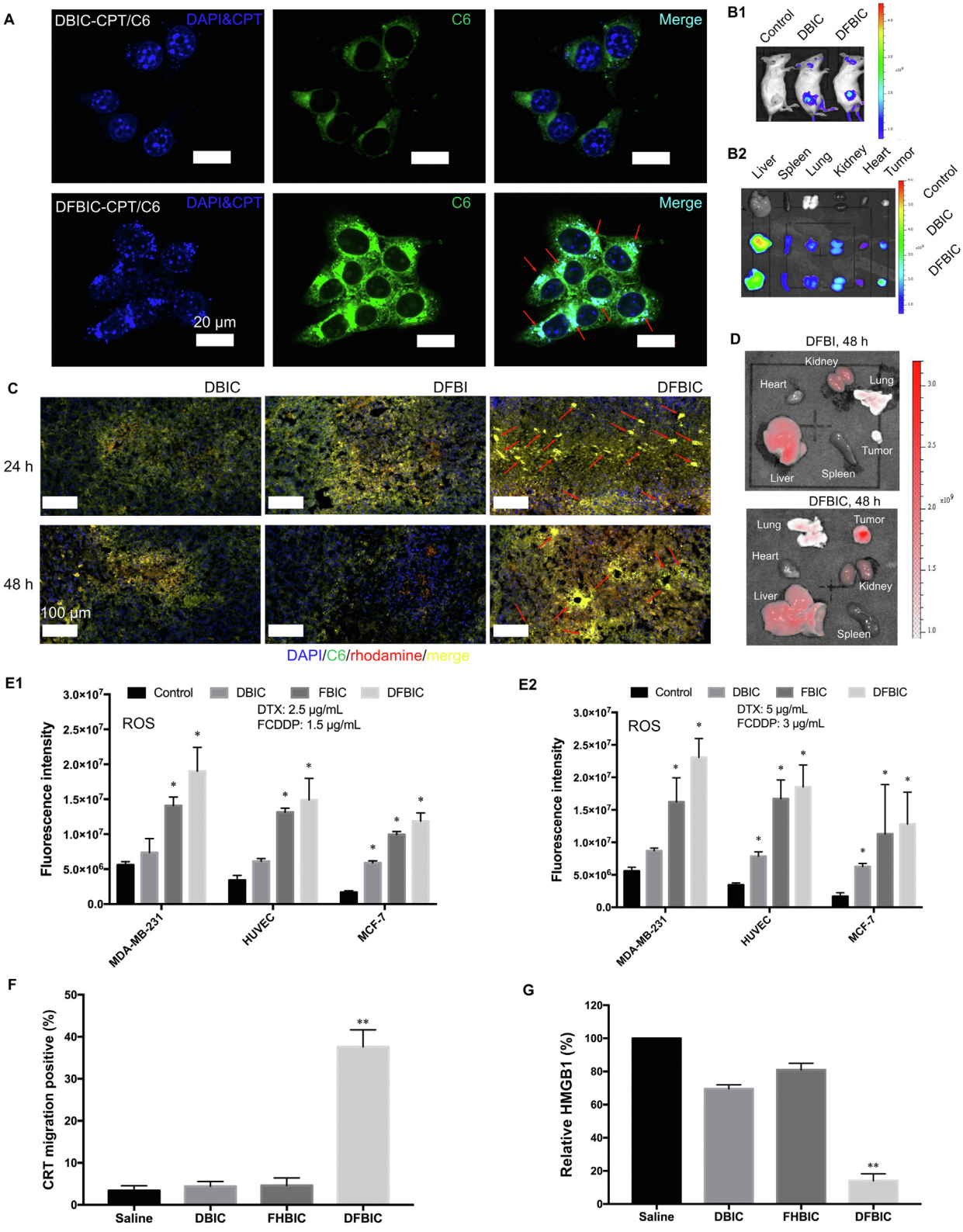

Figure 2 Intracellular immobilization of nanoassemblies *in vitro* and *in vivo*. (A) Intracellular aggregation of nanoassemblies in cancer cell *in vitro*. (B) Fluorescent images of the mice after treated with different nanoassemblies (B1) and the distribution of the nanoassemblies *in vivo* (B2). Tumor-targeting of the nanoassemblies *in vivo*. (C) Intracellular immobilization of nanoassemblies *in vivo*. Fluorescent images of the tumoric frozen section uncovered the intracellular aggregation of nanoassemblies inside tumor tissue. (D) Effect of ligand onto the retention of the nanoassemblies *in vivo*. (E) The ROS production of the MDA-MB-231 cell lines after incubated with control, DBIC, FBIC, DFBIC, respectively. The fluorescent intensity measured from different cell types incubated with different concentrations of nanoassemblies: left, 2.5 μg/mL (DTX, E1) and right, 5 μg/mL (DTX, E2) (mean ± SD, $n = 3$, $^*P < 0.05$, $^{**}P < 0.01$). (F) The proportion of cancer cells took place CRT migration *in vitro* after being treated with nanoassemblies (mean ± SD, $n = 3$, $^*P < 0.05$, $^{**}P < 0.01$). (G) The proportion of cancer cells took place HMGB1 migration *in vitro* after being treated with nanoassemblies (mean ± SD, $n = 3$, $^*P < 0.05$, $^{**}P < 0.01$).

Table 1 IC_{50} of drugs and nanoassemblies to different cell lines (unit: μg/mL).

Sample		Cell line								
		4T1 (24 h)	4T1-Lu (24 h)	4T1 (48 h)	231 (24 h)	231 (48 h)	HCT8[d] (24 h)	HCT8[d] (48 h)	HCT15[d] (24 h)	HCT15[d] (48 h)
FCDDP	FBIC[a]	11.6±0.6	12.5±0.7	–	–	–	–	–	–	–
	DBIC[b]	–	–	–	24.6±0.9	18.7±0.7	42±2.4	25±1.1	–	–
	DFBI[b]	8.8±0.3	–	–	18.6±0.4	–	–	–	–	–
	DFBIC[b]	4.6±0.4	–	–	16.9±0.7	9.1±0.5	19.4±0.9	9.4±0.4	24.7±1.3	1.9±0.1
	Free DTX[b]	–	–	–	–	–	>100	>100	–	–
HCDDP	HBI[c]	1.2±0.1	–	0.2±0.0	1.56±0.2	0.51±0.1	–	–	–	–
	HBIC[c]	0.64±0.1	–	0.21±0.0	1.63±0.1	0.54±0.0	–	–	–	–
FCDDP/ HCDDP	Free CDDP[b]	–	–	–	6.27±0.2	1.76±0.2	–	–	–	–
	DFHBIC[b]	–	–	–	1.78±0.1	<0.2	–	–	–	–

–Not applicable.
Each experiment was repeated 6 times, and the results were listed as mean ± SD.
[a]Concentration of FCDDP.
[b]Concentration of DTX.
[c]Concentration of HCDDP.
[d]PTX resistant cell lines.

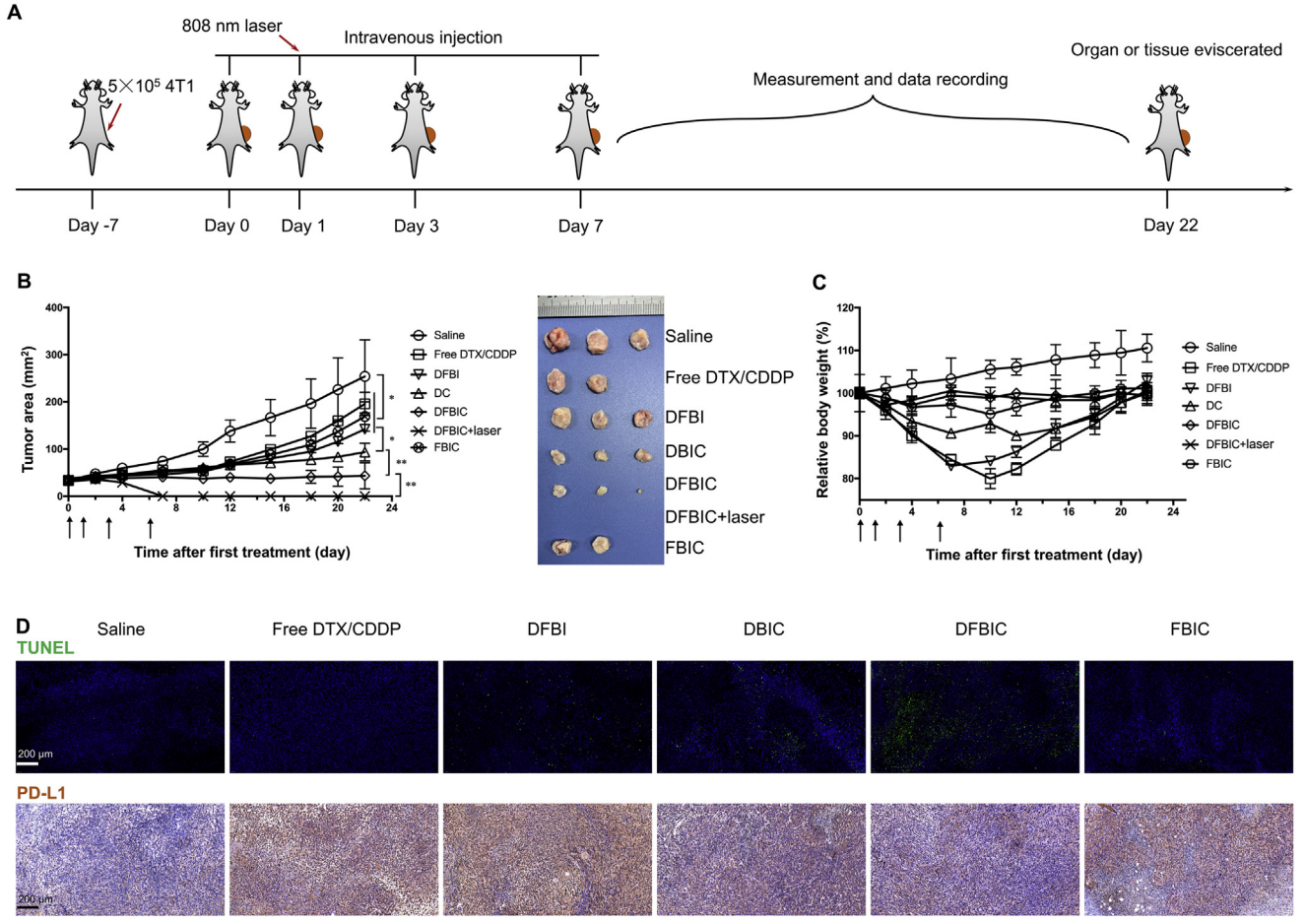

Figure 3 Anticancer performance of nanoassemblies *in vivo* (tumor volume: ~100 mm^3 while the first treatment was conducted). (A) Administration route. (B) Tumor area *versus* time (mean ± SD, $n = 3$, $^*P < 0.05$, $^{**}P < 0.01$). Inset: image of tumor tissues. (C) Body weight *versus* time (mean ± SD, $n = 3$, $^*P < 0.05$, $^{**}P < 0.01$). (D) Immunofluorescent staining (TUNEL) and immunohistochemical staining (αPD-L1) of tumor tissues.

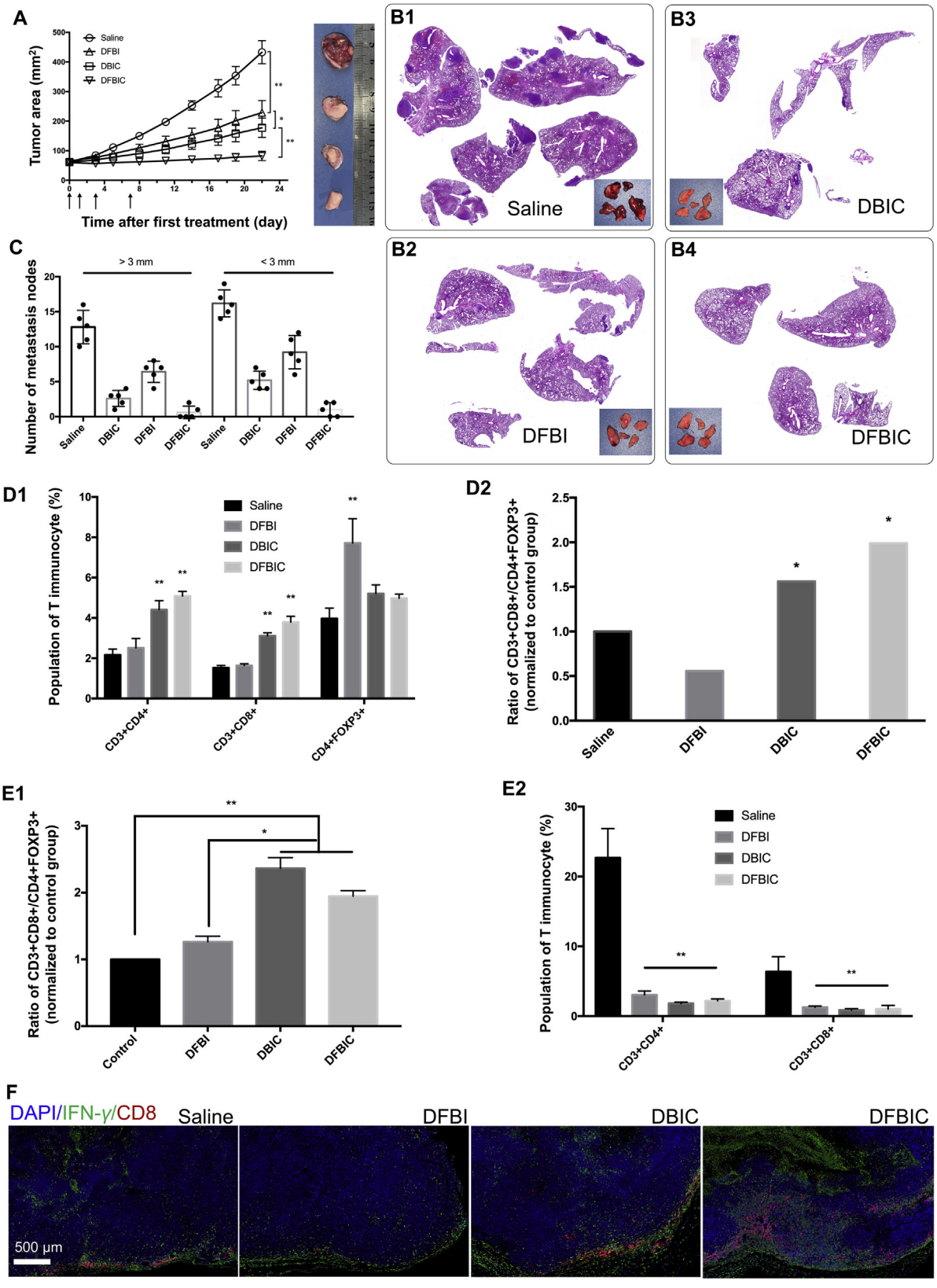

Figure 4 Pulmonary metastasis alleviation by nanoassemblies *in vivo* (tumor volume: ~250 mm^3 while the first treatment was conducted). (A) Tumor area versus time (mean ± SD, $n = 5$, $^*P < 0.05$, $^{**}P < 0.01$). Inset: representative images of the tumors eviscerated from each group. (B)

the peptide CF27 on the formation of intracellular aggregates *in vitro*. Both DFBI (without peptide modification) and DFBIC (with peptide modification) resulted in intracellular aggregation (Fig. S13). The fluorescence intensity (FI) observed in the DFBIC-treated groups was slightly stronger than that in the DFBI-treated groups, demonstrating the enhancement of cellular uptake by peptide reprogramming. In addition, in our previous study[35], we found that the expression of some proteins in cancer cells at different temperatures was different, which may affect the uptake of the nanoassembly by the cancer cells. Therefore, we further evaluated the effect of temperature on the intracellular aggregation of nanoassemblies. The results indicated that the uptake of the nanoassemblies by cancer cells may be reduced at higher temperatures (42 °C), but temperature changes have little effect on the intracellular aggregation of nanoassemblies.

3.3.2. *Intracellular aggregation in vivo*

We also further investigated whether the intracellular aggregation of the nanoassembly could be realized *in vivo*. Before we evaluated the intracellular aggregation of the nanoassemblies *in vivo*, we first investigated their tumor-targeting ability *in vivo*. Because of the incorporation of IR820, which can serve as an enhancer for fluorescence imaging, we then estimated the accumulation of the nanoassemblies in the tumor site *in vivo via* fluorescence imaging. Compared with the nanoassembly without FCDDP (DBIC), the DFBIC nanoassembly exhibited enhanced accumulation in the tumor site and enhanced tumor growth inhibition, based on the results of fluorescence and bioluminescence imaging at 48 h (Fig. 2B1 and Supporting Information Fig. S14). IR820 itself can serve as the NIR fluorescent dye. The 4T1-Lu cell line was used for bioluminescence imaging to evaluate tumor growth *in vivo*. By semiquantitatively measuring the FI of the tumor site *in vivo* in real time, we further confirmed the enhanced nanoassembly accumulation in the DFBIC-treated group (Fig. S14). Moreover, 48 h later, FI measurements of the eviscerated organs indicated that the average FI in the tumor tissues was even stronger than that in the liver and much stronger than that in the group treated with DBIC (Fig. 2B2). These results indicate that aggregation favors the accumulation of the nanoassembly in the tumor site.

Then, by directly observing frozen tumor sections after staining with DAPI, we can localize the intratumoral distribution of the nanoassemblies after intravenous injection. In addition, rhodamine can serve as a fluorescent dye, and we can then assess the colocalization of rhodamine and C6, which represents the nanoassemblies. Twenty-four hours after injection, obvious concentrated fluorescent puncta were found in tumor tissues from the group treated with DFBIC. A similar but lower proportion of puncta was found in the group treated with DFBI. However, no such distribution was observed in the group treated with DBIC, confirming that the introduction of FCDDP favored the formation of aggregation *in vivo* (Fig. 2C, upper row). After another 24 h, the FI was increased in both the DBIC- and DFBIC-treated groups but was attenuated in the DFBI-treated group. In the DFBIC-treated group, aggregation was enhanced (Fig. 2C, bottom row). These results demonstrate that aggregation of the DFBIC nanoassembly can also be achieved *in vivo*. Moreover, with peptide modification, enrichment of the nanoassembly in the tumor site was indeed enhanced (Supporting Information Fig. S15), which is mainly ascribed to the stimuli-responsive and tumor-targeting properties of CF27[30,37,38]. In the group treated with DFBI, which does not include the peptide modification, the FI of the tumor was reduced to a hardly detectable level (similar to that of the heart tissue, Fig. 2D). In contrast, the group treated with DFBIC still exhibited a strong fluorescence signal even after 48 h (Fig. 2D).

3.4. *Nanoassembly-induced reactive oxygen species (ROS) generation and immunogenic cell death (ICD)*

In addition, some of the components used to form nanoassemblies, *e.g.*, FCDDP and BISS, can consume intracellular GSH, which is a critical molecule to counterbalance ROS. The depletion of GSH results in the generation of ROS. After incubation with DFBIC, ROS were increased, indirectly indicating the consumption of GSH inside the tumor cells (Fig. 2E and Supporting Information Fig. S16). Furthermore, beyond the aggregation of the DFBIC nanoassembly achieved in the presence of GSH, the consequence of intracellular aggregation may affect cellular behaviors. After incubation with DFBIC, calreticulin (CRT) in the cancer cells (∼40%) migrated from the endoplasmic reticulum (where it is normally localized) to a specific location on the cell membrane (Fig. 2F and Supporting Information Fig. S17, upper row). Moreover, the FI of HMGB1 in cancer cells after incubation with DFBIC and labeling with an anti-HMGB1 antibody was much weaker than that in the other groups, including the PBS, DBIC, and FBIC groups (Fig. 2G and Fig. S17, bottom row). CRT migration combined with HMGB1 diffusion is the signature of ICD[39–41]. Taxanes only minimally induce ICD, whereas platinum-based chemotherapeutics such as oxaliplatin and carboplatin can induce ICD. The results in the FHBIC-treated group demonstrated that neither FCDDP nor HCDDP could induce ICD[42], but the combination of DTX and FCDDP (DFBIC) induced ICD. This finding verifies that DFBIC-induced aggregation remodels the intracellular environment, favoring the improved effects of immunotherapy mediated by ICD.

3.5. *In vitro cytotoxicity*

Two kinds of cisplatin prodrugs were synthesized in this study; thus, we estimated the cytotoxicity of the nanoassemblies formed from these two kinds of prodrugs. Two triple-negative breast cancer cell lines, 4T1 and MDA-MB-231 (231), were used as model cancer cells. In the absence of DTX, FBIC exhibited

H&E staining of lung tissues after treatments. Inset: images of lung tissues eviscerated from each groups. (C) The metastatic nodes calculated by visual inspecting (mean ± SD, $n = 5$, $^{*}P < 0.05$, $^{**}P < 0.01$). (D) The proportion of immunocytes in spleens after different treatments: D1, T cells; D2, ratios of $CD3^{+}CD8^{+}$ T cells and Treg ($CD4^{+}FOXP3^{+}$ T cells) (mean ± SD, $n = 3$, $^{*}P < 0.05$, $^{**}P < 0.01$). (E) The proportion of immunocytes in tumors after different treatments: E1, ratios of $CD3^{+}CD8^{+}$ T cells and $CD3^{+}CD4^{+}$ T cells); E2, T cells (mean ± SD, $n = 3$, $^{*}P < 0.05$, $^{**}P < 0.01$). (F) Immunofluorescent staining of tumor tissues for enhanced immunotherapy evaluation. Tumor tissues were all co-stained with DAPI, αCD8 and αIFN-γ.

obvious cytotoxicity to the 4T1 cell line when the FCDDP concentration was higher than 12.5 μg/mL. Without FCDDP, DBIC exhibited obvious cytotoxicity to the 231 cell line at 24 and 48 h only when the DTX concentration was higher than 25 μg/mL. The introduction of FCDDP enhanced the toxicity of DBIC to the 231 cell line (a dramatic reduction in the mean cell survival rate was observed at a DTX concentration of 12.5 μg/mL and an FCDDP concentration of 7.5 μg/mL). The CF27 peptide modification had little effect on the cytotoxicity of the DFBI nanoassembly. However, both nanoassembly formulations, DBIC and DFBIC, indeed reversed the cytotoxicity of DTX to the cancer cell line with paclitaxel (PTX) resistance. An obvious reduction was observed in the mean cell survival rate of HCT8 cells (PTX-resistant) treated with DBIC or DFBIC, while only a slight reduction was found in the group treated with free DTX (Table 1 and Supporting Information Fig. S18). Similar cytotoxicity was observed in another PTX-resistant cancer cell line, HCT15 (PTX-resistant, Table 1). The results demonstrated that the DFBIC nanoassemblies can affect the proliferation of several types of drug-resistant cancer cells.

Regarding the HCDDP-based nanoassemblies, HBI and HBIC exhibited obvious cytotoxicity to 4T1 and 231 cells, similar to the findings in other reports (Table 1 and Fig. S18)[43]. Then, we coencapsulated FCDDP and HCDDP into the nanoassembly and found that the combination of these two cisplatin prodrugs greatly enhanced the cytotoxicity of the nanoassembly to both the 4T1 and 231 cancer cell lines (Table 1 and Fig. S18). These results demonstrated that this modification had a critical effect not only on the reaction of the prodrugs with the reductant but also on the cytotoxicity of the cisplatin-based nanoassemblies. The reaction rate of the prodrugs with the reductant controlled the aggregation. If the reaction rate was slow, the nanoassembly could dissociate, leading to failure of aggregation.

3.6. *Anticancer growth in vivo*

Then, we established a triple-negative breast cancer model in BALB/c mice by subcutaneously injecting 5×10^5 4T1 breast cancer cells into the right flank of each mouse. When the average size of the tumors reached ~100 mm^3 (6 mm × 6 mm), the tumor-bearing mice were divided into several groups and treated with PBS, free DTX plus CDDP, DFBI, DBIC, DFBIC, and FBIC. The doses of DTX and CDDP prodrugs or CDDP were 10 and 3 mg/kg body weight (equal to moles of CDDP), respectively. For further evaluation, a group treated with DFBIC combined with 808 nm laser irradiation (DFBIC+Laser) was also established. The first treatment was administered on Day 0, and the mice were further intravenously injected with the specific formulations on Days 0, 1, 3, and 6 (Fig. 3A). No obvious additional tumor growth was detected in the group treated with DFBIC (the tumor growth inhibition rate was ~85%). The tumor inhibition rate in the group treated with DBIC was ~60%, which was higher than that in the groups treated with DFBI (~45%), FBIC (~33%) and free DTX/CDDP (~23%). No significant difference was found among the DFBI- and FBIC- and free DTX/CDDP-treated groups (Fig. 3B). Moreover, the group treated with DFBIC combined with 808 nm laser irradiation exhibited total tumor elimination, and no recurrence occurred during the assay, similar to the results in some of our previous studies[36,44,45]. The photograph of the tumors eviscerated on Day 22 more clearly shows the differences in tumor growth inhibition in the groups treated with different formulations. Furthermore, by recording the body weight of the mice during the treatment and recording period, we found that the group treated with the free forms of the drugs exhibited severe weight loss in the initial stage, which was slowly recovered in the later stage. Similar weight loss was observed in the group treated with DFBI. No significant weight loss was observed in the DFBIC-, DFBIC+Laser-, and FBIC-treated groups. Slight weight loss was detected in the DBIC-treated group, but this loss was much milder than that in the free form- or DFBI-treated groups (Fig. 3C). These results not only demonstrate the low toxicity of FCDDP but also reveal that peptide modification or reprogramming of the nanoassembly could alter the adverse effects caused by chemotherapeutics.

The tumor growth inhibition induced by DFBIC may be related to the ability of this nanoassembly to induce cancer cell apoptosis *in vivo*. After treatment, the apoptosis index was much higher than 75%, higher than that in the DBIC-treated group (~56%), and much higher than that in the other groups: PBS, ~11%; free DTX/CDDP, ~17%; DFBI, ~21%; and FBIC, ~16% (Fig. 3D, upper row). In addition, we found that chemotherapy may elevate the expression of PD-L1. After treatment with free DTX/CDDP, the percentage of cancer cells with high PD-L1 expression increased from ~23% (as observed in the saline-treated group) to ~82%, and a similar result was found in the DFBI- and FBIC-treated groups. In the groups treated with DBIC and DFBIC, PD-L1 expression levels were ~36% and ~28%, respectively, due to the ability of the CF27 peptide to block PD-1/PD-L1[30,46]. Chemotherapy may promote tumor cell aggressiveness and invasiveness, and PD-L1 promotes metastasis. Attenuation of PD-L1 expression by DFBIC favors stabilization of the primary tumor and lowers the risk of invasion and metastasis.

3.7. *Alleviated pulmonary metastasis and enhanced immunotherapy*

More importantly, we confirmed that DFBIC can induce ICD-like cancer cell behavior in an *in vitro* assay. This finding indicates that DFBIC may enhance the immunotherapy-mediated alleviation of metastasis. We further established a 4T1 breast cancer model in BALB/c mice (2×10^6 cells per mouse, implanted subcutaneously) and treated the mice with saline, DFBI, DBIC, or DFBIC when the tumor volumes reached ~250 mm^3 (8 × 8 mm). Similar primary tumor growth inhibition was observed (Fig. 4A). Severe lung metastasis was observed in the saline-treated group, and metastasis was alleviated but still occurred in the DFBI-treated group. The group treated with DBIC exhibited further alleviation of lung metastasis, and H&E staining of lung tissues and the number of metastatic nodes further demonstrated that DFBIC treatment not only effectively inhibited primary tumor growth but also greatly alleviated lung metastasis (Fig. 4B and C). In our previous study, we confirmed that the CF27 peptide could reinvigorate the immune system to inhibit tumor growth and metastasis by blocking the PD-1/PD-L1 immune checkpoint. This ability can explain the alleviation of metastasis in the group treated with DBIC. The enhanced alleviation of lung metastasis in the DFBIC-treated group may be ascribed to the combination of ICD and PD-1/PD-L1 blockade and was connected mainly with stimulation of the immune system.

Although several theories for immunotherapy have been developed and numerous cell types and cytokines are related to immunotherapy, in this study, we identified variations in T cell

subtypes, including $CD3^+CD4^+$ T cells and $CD3^+CD8^+$ T cells as well as $CD25^+FOXP3^+$ T cells (Tregs), in spleens removed from mice after different treatments. In the groups treated with DBIC and DFBIC, the proportions of both $CD3^+CD4^+$ T cells and $CD3^+CD8^+$ T cells increased after treatment. In addition, the population of Tregs in the group treated with DFBI was nearly twice that in the control group, while the population of Tregs in the groups treated with DBIC and DFBIC was hardly affected (Fig. 4D and Supporting Information Fig. S19). Consequently, the ratios of $CD8^+$ T cells to Tregs in the DBIC- and DFBIC-treated groups were much higher than those in the DFBI-treated group and the control group. This pattern demonstrates that a systemic immune response was elicited by DFBIC treatment. Although the differences in the populations of immunocytes between the DBIC-treated group and the DFBIC-treated group were not significant, DFBIC more effectively stimulated the immune response and alleviated adverse effects. Nevertheless, analysis of the immunocyte population in tumor tissues revealed that the proportions of both $CD3^+CD4^+$ T cells and $CD3^+CD8^+$ T cells were greatly decreased in the chemotherapeutic-treated groups, indicating that the chemotherapeutics indeed damaged the intratumoral immune system (Fig. 4E and Supporting Information Fig. S20). However, the ratios of $CD8^+$ T cells to $CD4^+$ T cells in the DFBIC- and DBIC-treated groups were higher than those in the control group and DFBI-treated group. By examining the slices of the tumor tissues after staining with aCD8 and aIFN-γ, we found reduced numbers of CD8-positive T cells in the free drug-, DFBI- and FBIC-treated groups. In both the DBIC- and DFBIC-treated groups, the migration ability of $CD8^+$ T cells was partially recovered after treatment, and this recovery was further enhanced in the DFBIC-treated group (Fig. 4F and Supporting Information Fig. S21). The nanoassembly could not repair the immunocyte damage induced by the chemotherapeutics but did enhance the chemotherapeutic outcome and potentiate the systemic immune response to alleviate pulmonary metastasis.

4. Conclusions

In summary, we used the cisplatin prodrug as the GSH-activated linker and a nanoassembly formed from combinations of cisplatin prodrugs/IR820/chemotherapeutics to develop a strategy for intracellular immobilization of nanomedicines. Under catalysis by GSH, the cisplatin prodrugs could be activated to react with the mercapto groups generated from the nanoassemblies, which then induced aggregation. This strategy enhanced the retention of the nanomedicines inside tumor cells and altered the apoptotic behavior of cancer cells, thus enhancing chemotherapeutic activity. In addition, a peptide with moieties for tumor-targeting and PD-1/PD-L1 blockade could be grafted onto the nanoassembly to achieve enhanced tumor-targeting and immunotherapeutic activity. GSH-induced intracellular aggregation not only enhanced the therapeutic activity of chemotherapeutics *in vitro* and *in vivo* but also favored the alleviation of pulmonary metastasis by reinvigorating immunocytes. This nanoassembly provides a promising strategy for the intracellular immobilization of nanoparticles both *in vitro* and *in vivo*.

Acknowledgments

This work was financially supported by the State Key Program of National Natural Science Foundation of China (31930067), the National Natural Science Fund for Distinguished Young Scholar (NSFC31525009, China), National Natural Science Funds (NSFC31771096, NSFC31871008, and NSFC31500809, China), the China Postdoctoral Science Foundation (2018M643484), 1·3·5 project for disciplines of excellence, West China Hospital, Sichuan University (ZYGD18002, China), and the Post-Doctor Research Project, West China Hospital, Sichuan University (18HXBH038, China).

Author contributions

Jinrong Peng, and Zhiyong Qian designed the research. Jinrong Peng, Yao Xiao, Qingya Liu, Qian Yang, Yu Chen, and Ruxia Han carried out the experiments and performed data analysis. Kun Shi and Ying Hao participated part of the experiments. Jinrong Peng and Zhiyong Qian wrote the manuscript. Jinrong Peng and Zhiyong Qian revised the manuscript. All of the authors have read and approved the final manuscript.

Conflicts of interest

The authors have no conflicts of interest to declare.

Appendix A. Supporting information

Supporting data to this article can be found online at https://doi.org/10.1016/j.apsb.2020.06.013.

References

1. Bertrand N, Wu J, Xu X, Kamaly N, Farokhzad OC. Cancer nanotechnology: the impact of passive and active targeting in the era of modern cancer biology. *Adv Drug Deliv Rev* 2014;**66**:2–25.
2. Li S, Zhang Y, Wang J, Zhao Y, Ji T, Zhao X, et al. Nanoparticle-mediated local depletion of tumour-associated platelets disrupts vascular barriers and augments drug accumulation in tumours. *Nat Biomed Eng* 2017;**1**:667–79.
3. Wang Z, Ju Y, Ali Z, Yin H, Sheng F, Lin J, et al. Near-infrared light and tumor microenvironment dual responsive size-switchable nanocapsules for multimodal tumor theranostics. *Nat Commun* 2019;**10**:4418.
4. Huynh E, Leung BYC, Helfield BL, Shakiba M, Gandier J-A, Jin CS, et al. *In situ* conversion of porphyrin microbubbles to nanoparticles for multimodality imaging. *Nat Nanotechnol* 2015;**10**:325–32.
5. Liu J, Ai X, Zhang H, Zhuo W, Mi P. Polymeric micelles with endosome escape and redox-responsive functions for enhanced intracellular drug delivery. *J Biomed Nanotechnol* 2019;**15**:373–81.
6. Liu R, Hu C, Yang Y, Zhang J, Gao H. Theranostic nanoparticles with tumor-specific enzyme-triggered size reduction and drug release to perform photothermal therapy for breast cancer treatment. *Acta Pharm Sin B* 2019;**9**:410–20.
7. Jain RK, Stylianopoulos T. Delivering nanomedicine to solid tumors. *Nat Rev Clin Oncol* 2010;**7**:653–64.
8. Wilhelm S, Tavares AJ, Dai Q, Ohta S, Audet J, Dvorak HF, et al. Analysis of nanoparticle delivery to tumours. *Nat Rev Mater* 2016;**1**:16014.
9. Chen H, Zhang W, Zhu G, Xie J, Chen X. Rethinking cancer nanotheranostics. *Nat Rev Mater* 2017;**2**:17024.
10. Vasan N, Baselga J, Hyman DM. A view on drug resistance in cancer. *Nature* 2019;**575**:299–309.
11. Yuan Y, Zhang J, Qi X, Li S, Liu G, Siddhanta S, et al. Furin-mediated intracellular self-assembly of olsalazine nanoparticles for enhanced magnetic resonance imaging and tumour therapy. *Nat Mater* 2019;**18**:1376–83.
12. Mi P, Cabral H, Kataoka K. Ligand-installed nanocarriers toward precision therapy. *Adv Mater* 2020;**32**:1902604.

13. Zhao Z, Ukidve A, Gao Y, Kim J, Mitragotri S. Erythrocyte leveraged chemotherapy (ELeCt): nanoparticle assembly on erythrocyte surface to combat lung metastasis. *Sci Adv* 2019;**5**:eaax9250.
14. Goldberg MS. Improving cancer immunotherapy through nanotechnology. *Nat Rev Cancer* 2019;**19**:587−602.
15. Yuan Y, Wang L, Du W, Ding Z, Zhang J, Han T, et al. Intracellular self-assembly of Taxol nanoparticles for overcoming multidrug resistance. *Angew Chem Int Ed* 2015;**54**:9700−4.
16. An HW, Li LL, Wang Y, Wang Z, Hou D, Lin YX, et al. A tumour-selective cascade activatable self-detained system for drug delivery and cancer imaging. *Nat Commun* 2019;**10**:4861.
17. Zhan J, Cai Y, He S, Wang L, Yang Z. Tandem molecular self-assembly in liver cancer cells. *Angew Chem Int Ed* 2018;**57**:1813−6.
18. Li J, Shi K, Sabet ZF, Fu W, Zhou H, Xu S, et al. New power of self-assembling carbonic anhydrase inhibitor: short peptide-constructed nanofibers inspire hypoxic cancer therapy. *Sci Adv* 2019;**5**:eaax0937.
19. Ding Z, Sun H, Ge S, Cai Y, Yuan Y, Hai Z, et al. Furin-controlled Fe_3O_4 nanoparticle aggregation and 19F signal "turn-on" for precise MR imaging of tumors. *Adv Funct Mater* 2019;**29**:1903860.
20. Ruan S, Yuan M, Zhang L, Hu G, Chen J, Cun X, et al. Tumor microenvironment sensitive doxorubicin delivery and release to glioma using angiopep-2 decorated gold nanoparticles. *Biomaterials* 2015;**37**:425−35.
21. Liu R, Yu M, Yang X, Umeshappa CS, Hu C, Yu W, et al. Linear chimeric triblock molecules self-assembled micelles with controllably transformable property to enhance tumor retention for chemo-photodynamic therapy of breast cancer. *Adv Funct Mater* 2019;**29**:1808462.
22. Peng J, Yang Q, Shi K, Xiao Y, Wei X, Qian Z. Intratumoral fate of functional nanoparticles in response to microenvironment factor: implications on cancer diagnosis and therapy. *Adv Drug Deliv Rev* 2019;**143**:37−67.
23. Balendiran GK, Dabur R, Fraser D. The role of glutathione in cancer. *Cell Biochem Funct* 2004;**22**:343−52.
24. Liu T, Liu Z, Chen J, Jin R, Bai Y, Zhou Y, et al. Redox-responsive supramolecular micelles for targeted imaging and drug delivery to tumor. *J Biomed Nanotechnol* 2018;**14**:1107−16.
25. Li M, Zhao L, Zhang T, Shu Y, He Z, Ma Y, et al. Redox-sensitive prodrug nanoassemblies based on linoleic acid-modified docetaxel to resist breast cancers. *Acta Pham Sin B* 2019;**9**:421−32.
26. Wang Z, Wang N, Cheng S-C, Xu K, Deng Z, Chen S, et al. Phorbiplatin, a highly potent Pt(IV) antitumor prodrug that can be controllably activated by red light. *Chem* 2019;**5**:3151−65.
27. Xu Y, Han X, Li Y, Min H, Zhao X, Zhang Y, et al. Sulforaphane mediates glutathione depletion *via* polymeric nanoparticles to restore cisplatin chemosensitivity. *ACS Nano* 2019;**13**:13445−55.
28. Qian Q, Zhu L, Zhu X, Sun M, Yan D. Drug-polymer hybrid macromolecular engineering: degradable PEG integrated by platinum(IV) for cancer therapy. *Matter* 2019;**1**:1618−30.
29. XI Z, LIU Y. Molecular mechanisms of cisplatin resistance. *Sci Sin Chim* 2014;**44**:410−22.
30. Peng J, Yang Q, Xiao Y, Shi K, Liu Q, Hao Y, et al. Tumor microenvironment responsive drug-dye-peptide nanoassembly for enhanced tumor-targeting, penetration, and photo-chemo-immunotherapy. *Adv Funct Mater* 2019;**29**:1900004.
31. Ellis LT, Er HM, Hambley TW. The influence of the axial ligands of a series of platinum(IV) anti-cancer complexes on their reduction to platinum(II) and reaction with DNA. *Aust J Chem* 1995;**48**:793−806.
32. Hu CM, Fang RH, Wang KC, Luk BT, Thamphiwatana S, Dehaini D, et al. Nanoparticle biointerfacing by platelet membrane cloaking. *Nature* 2015;**526**:118−21.
33. Hu CM, Zhang L, Aryal S, Cheung C, Fang RH, Zhang L. Erythrocyte membrane-camouflaged polymeric nanoparticles as a biomimetic delivery platform. *Proc Natl Acad Sci U S A* 2011;**108**:10980−5.
34. Yuan YY, Mao CQ, Du XJ, Du JZ, Wang F, Wang J. Surface charge switchable nanoparticles based on zwitterionic polymer for enhanced drug delivery to tumor. *Adv Mater* 2012;**24**:5476−80.
35. Shamay Y, Shah J, Işık M, Mizrachi A, Leibold J, Tschaharganeh DF, et al. Quantitative self-assembly prediction yields targeted nanomedicines. *Nat Mater* 2018;**17**:361−8.
36. Peng J, Xiao Y, Li W, Yang Q, Tan L, Jia Y, et al. Photosensitizer micelles together with IDO inhibitor enhance cancer photothermal therapy and immunotherapy. *Adv Sci* 2018;**5**:1700891.
37. Huang X, Yin Y, Wu M, Zan W, Yang Q. LyP-1 peptide-functionalized gold nanoprisms for SERRS imaging and tumor growth suppressing by PTT induced-hyperthermia. *Chin Chem Lett* 2019;**30**:1335−40.
38. Chen C, Li Y, Yu X, Jiang Q, Xu X, Yang Q, et al. Bone-targeting melphalan prodrug with tumor-microenvironment sensitivity: Synthesis, *in vitro* and *in vivo* evaluation. *Chin Chem Lett* 2018;**29**:1609−12.
39. Green DR, Ferguson T, Zitvogel L, Kroemer G. Immunogenic and tolerogenic cell death. *Nat Rev Immunol* 2009;**9**:353−63.
40. Chen L, Chen L, Qin Z, Lei J, Ye S, Zeng K, et al. Upregulation of miR-489-3p and miR-630 inhibits oxaliplatin uptake in renal cell carcinoma by targeting OCT2. *Acta Pham Sin B* 2019;**9**:1008−20.
41. Obeid M, Tesniere A, Ghiringhelli F, Fimia GM, Apetoh L, Perfettini JL, et al. Calreticulin exposure dictates the immunogenicity of cancer cell death. *Nat Med* 2007;**13**:54−61.
42. Wan X, Min Y, Bludau H, Keith A, Sheiko SS, Jordan R, et al. Drug combination synergy in worm-like polymeric micelles improves treatment outcome for small cell and non-small cell lung cancer. *ACS Nano* 2018;**12**:2426−39.
43. Galluzzi L, Senovilla L, Zitvogel L, Kroemer G. The secret ally: immunostimulation by anticancer drugs. *Nat Rev Drug Discov* 2012;**11**:215−33.
44. Peng J, Yang Q, Li W, Tan L, Xiao Y, Chen L, et al. Erythrocyte-membrane-coated Prussian blue/manganese dioxide nanoparticles as H_2O_2-responsive oxygen generators to enhance cancer chemotherapy/photothermal therapy. *ACS Appl Mater Interfaces* 2017;**9**:44410−22.
45. Yang Q, Peng J, Xiao Y, Li W, Tan L, Xu X, et al. Porous Au@Pt nanoparticles: Therapeutic platform for tumor chemo-photothermal co-therapy and alleviating doxorubicin-induced oxidative damage. *ACS Appl Mater Interfaces* 2018;**10**:150−64.
46. Yang Q, Peng J, Shi K, Xiao Y, Liu Q, Han R, et al. Rationally designed peptide-conjugated gold/platinum nanosystem with active tumor-targeting for enhancing tumor photothermal-immunotherapy. *J Control Release* 2019;**308**:29−43.